

Cite this: *J. Mater. Chem. C*, 2017,  
5, 12023Received 28th August 2017,  
Accepted 23rd October 2017

DOI: 10.1039/c7tc03905k

rsc.li/materials-c

# Molecular doping in organic semiconductors: fully solution-processed, vacuum-free doping with metal–organic complexes in an orthogonal solvent†

Ryo Fujimoto,<sup>‡</sup> Yu Yamashita,<sup>‡</sup> Shohei Kumagai,<sup>ib</sup> Junta Tsurumi,<sup>a</sup>  
Alexander Hinderhofer,<sup>b</sup> Katharina Broch,<sup>b</sup> Frank Schreiber,<sup>ib</sup>  
Shun Watanabe,<sup>ib</sup>\*<sup>ac</sup> and Jun Takeya,<sup>ib</sup><sup>a</sup>

**Chemical doping in  $\pi$ -conjugated organic semiconductors, which involves a redox reaction between a host  $\pi$ -conjugated material and a dopant, is achieved by either co-evaporation, co-dissolved solution, or exposure to a dopant gas. Here, we demonstrate a new route for molecular doping; a thiophene-based semiconducting polymer film can be doped with dopants dispersed in an orthogonal solvent. An increase in conductivity is demonstrated as a result of adopting a strong acceptor dopant, a metal–organic complex, to achieve an efficient charge transfer because the introduced dopant is likely to reside within the polymer lamellae throughout the entire bulk of the organic semiconductor film. Comprehensive magneto-transport and spectroscopic studies confirm that band-like transport is realized in such dopant-implanted conducting polymers. The present method can shed light on molecular doping in materials science because any molecular dopants that are non-evaporative and insoluble can be used with this method.**

## Introduction

The discovery of plastic-based conductors, such as polyacetylene<sup>1</sup> and polyaniline,<sup>2</sup> has revolutionized conventional inorganic-based electronics. Such  $\pi$ -conjugated polymeric conductors can be produced *via* a simple, solution process onto any given substrate including ultra-thin, flexible substrates to offer a wider variety of functionalities with applications such as a substitutional conductor, for example as hole transport layers in solar cells,<sup>3</sup> as cathodes in supercapacitors,<sup>4</sup> and as media in gas/bio-sensors.<sup>5</sup>

Their potential is nowadays highlighted in terms of various advanced applications, such as a significantly large thermo-electric figure-of-merit demonstrated for a thiophene-based conducting polymer,<sup>6</sup> and an inverse spin Hall-effect, which converts a spin signal to an electromotive force, was also demonstrated in a solution processed conducting polymer.<sup>7</sup> The main drawback is that the materials or methods used to realize a reasonably high conductivity have been limited to date; to the best of our knowledge, materials in the poly(3,4-ethylenedioxythiophene) (PEDOT) family are the only materials that have both excellent device performance and solution processability.

In most semiconductor processing strategies, doping is the most indispensable building block that enables both charge concentration and electrical conductivity to be tuned. In inorganic semiconductors, doping is achieved by implanting impurity dopants, by which the Fermi energy is controlled. Doping in  $\pi$ -conjugated materials is rather complicated; they involve polaron formation either *via* oxidation (for p-type) or *via* reduction (for n-type).<sup>8,9</sup> A  $\pi$ -conjugated core is distorted by the addition or extraction of electrons, so structural and energetic disorder is unavoidable. In chemical doping where halogens such as bromine and iodine<sup>1</sup> are utilized, relatively strong chemisorption can cause uncontrollable structural hybridization. Electrochemical doping enables precise control of the redox in conjugated polymers.<sup>6,8</sup> However, the use of an electrochemical cell is limited because dopants should form an electrolyte. Although electrostatic doping using a field-effect transistor is the most accurate way to tune the doping level, the doping level is small compared to other doping methods. Most recently, doping with molecular-based dopants has been extensively studied,<sup>10–12</sup> where a dopant is mixed into a host  $\pi$ -conjugated material, and the dopant either donates an electron to the host (n-type doping), or accepts an electron from the host (p-type doping). Molecular doping is processed by various methods, such as co-evaporation of the host and dopant in a vacuum, mixing the dopant into a solution of the host organic semiconductor (then deposition of the dopant-mixed solution

<sup>a</sup> Material Innovation Research Center (MIRC) and Department of Advanced Materials Science, Graduate School of Frontier Sciences, The University of Tokyo, 5-1-5 Kashi-wanoha, Kashiwa, Chiba 277-8561, Japan.  
E-mail: swatanabe@edu.k.u-tokyo.ac.jp

<sup>b</sup> Institut für Angewandte Physik, Universität Tübingen, Auf der Morgenstelle 10, 72076 Tübingen, Germany

<sup>c</sup> JST, PRESTO, 4-1-8 Honcho, Kawaguchi, Saitama, 332-0012, Japan

† Electronic supplementary information (ESI) available. See DOI: 10.1039/c7tc03905k

‡ These authors contributed equally to this work.

by a method such as spin-coating), or exposure of the host organic semiconductor film/crystal to a gas of the dopant.<sup>9</sup> In such cases, the original molecular structure of the host organic semiconductor can be distorted by the dopant. More recently, we have developed a novel doping method, molecular implantation, which enables the introduction of a dopant into the semiconducting polymer network. Molecular implantation is a top-down type of doping method, which involves a solid-state diffusion process. The dopant is thermally evaporated directly onto the top of the semiconducting layers, and the deposited dopants diffuse all the way into the bulk of the semiconducting layer.<sup>13</sup> In contrast to conventional chemical doping methods where an admixture of dopants results in structural disorder in the host polymer,<sup>10–12</sup> molecular implantation rather improves the original lamellar structure because the dopants are likely to reside in-between each lamellae. In addition, a relatively large charge concentration of up to  $5 \times 10^{20} \text{ cm}^{-3}$  is achieved with excellent controllability of the doping level.<sup>14</sup> Although molecular implantation is considered to be an ideal method for the molecular doping of organic semiconductors, it requires a vacuum process, so dopant molecules have been limited to only those that are evaporative small molecules.

Here, we extend the concept of molecular implantation, and present a simpler, versatile and efficient doping method. A standard thiophene-based polymeric semiconductor, poly(2,5-bis(3-tetradecylthiophen-2-yl)thieno[3.2-*b*]thiophene) (PBTTT-C14), can be doped by various dopants in solution, where dopants are not necessarily fully dissolved in the solvent. A solid-state film of PBTTT-C14 was immersed into a dopant-dispersed fluorinated solvent CT-solv 180™ (commercially available from Asahi Glass Co.), which is commonly used to dilute the fluorinated insulating polymer CYTOP™. Efficient charge transfer and reasonably high electrical conductivity were demonstrated with two different molecular dopants, 2,3,5,6-tetrafluoro-7,7,8,8-tetracyanoquinodimethane (F4-TCNQ) and molybdenum tris(1-(trifluoroacetyl)-2-(trifluoromethyl)ethane-1,2-dithiolene) (Mo(tfd-COCF<sub>3</sub>)<sub>3</sub>). It should be noted that even with non-evaporative, insoluble dopants such as the Mo(tfd-COCF<sub>3</sub>)<sub>3</sub> metal-organic complex, a significant increase in conductivity together with a metallic nature, *i.e.* observation of the Hall effect and Anderson localization, is confirmed. Comprehensive studies based on UV-vis-NIR absorption, electron spin resonance (ESR) spectroscopy, and X-ray reflectivity (XRR) measurements confirm that dopant molecules are likely stored within the lamellae in PBTTT-C14, which enables two-dimensional charge transport to be established.

## Results and discussion

To assess the degree of doping in the standard PBTTT-C14/F4-TCNQ system, three different methods were tested: (i) conventional molecular implantation, where the dopant F4-TCNQ is thermally-evaporated directly on top of the PBTTT-C14 layer,<sup>13,14</sup> (ii) dopant-dissolved polar solution (F4-TCNQ dissolved in acetonitrile), and (iii) dopant-dispersed non-polar solution (F4-TCNQ dispersed in CT-solv 180). For (ii) and (iii), the PBTTT-C14 thin film

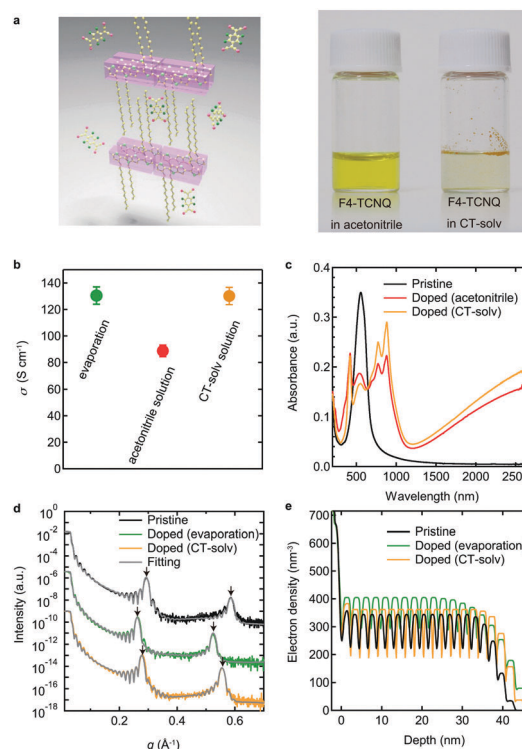


**Fig. 1** (a) A schematic of the proposed doping method; a thin film of PBTTT-C14 is immersed into the dopant-dispersed orthogonal solvent. The dopant, F4-TCNQ, dispersed in CT-solv 180 intercalates into the bulk of PBTTT-C14 (left). A photograph of dopant F4-TCNQ-dissolved acetonitrile, and F4-TCNQ-dispersed CT-solv (right), where the concentration was fixed to 1.5 wt%. (b) Variation in conductivity for three samples: PBTTT-C14 doped by conventional thermal evaporation (green), doped in acetonitrile (red), and doped in CT-solv 180 (orange). Note that the conductivity of the pristine (undoped) PBTTT was found to be on the order of  $10^{-4} \text{ S cm}^{-1}$ . (c) UV-vis-NIR absorption spectra obtained for pristine PBTTT-C14 (black), PBTTT-C14 doped in acetonitrile (red), and PBTTT-C14 doped in CT-solv 180 (orange). (d) XRR profile of pristine PBTTT-C14 (black), PBTTT-C14 doped by evaporation (green), and PBTTT-C14 doped in CT-solv (orange). Arrows denote the Bragg peaks corresponding to (*h*00) diffraction due to the lamellar spacing of PBTTT. Gray curves represent the fitting results based on the Parratt formalism. (e) Depth profile of the electron density. All measurements were performed at room temperature.

was immersed into the dopant solution with tuning of the process temperature (Fig. 1a). For polar solvents such as acetonitrile, F4-TCNQ is fully dissolved up to approximately 5 wt%, whereas the solubility of F4-TCNQ in non-polar solvents such as the fluorinated CT-solv 180 solvent is almost zero (see the photograph in Fig. 1a). Fig. 1b shows the variation in conductivity for samples doped *via* the three different methods. The process temperatures for (ii) acetonitrile and for (iii) CT-solv 180 were optimized to 60 and 110 °C, respectively (details are shown in the ESI,† Fig. S1). The conductivity measured for the sample doped in dopant-dispersed CT-solv 180 (*ca.*  $130 \text{ S cm}^{-1}$ ) was comparably large relative to that achieved by conventional evaporation doping, and was larger than that doped in acetonitrile. This is presumably because the higher process temperature for doping in CT-solv 180 promotes thermal energy for F4-TCNQ to

migrate into an energetically-favorable location in the bulk of PBTTT-C14. In addition, moderate heating may swell the lamellae of the PBTTT-C14 thin film, which promotes the intercalation of F4-TCNQ. A wider process temperature window, which is due to a higher boiling point for CT-solv, can be advantageous to adjust the doping efficiency. The degree of doping was confirmed by UV-vis-NIR absorption spectroscopy. Fig. 1c shows UV-vis-NIR absorption spectra obtained for the pristine PBTTT-C14 film (black), (ii) PBTTT-C14 doped in acetonitrile (red) and (iii) PBTTT-C14 doped in CT-solv 180 (orange). After the PBTTT-C14 film is doped (red/orange spectra), the absorption at 550 nm, which corresponds to the energy transfer between  $\pi$  and  $\pi^*$  orbitals in PBTTT-C14, is bleached, and doublets at 767 and 830 nm and a broad tail at 1500–2500 nm appear. The former is assigned to the absorption of fully ionized F4-TCNQ and the latter to the polaron absorption of PBTTT-C14,<sup>13,14</sup> both of which are considered to be a good index of the degree of doping.<sup>10,13,14</sup> The features in (iii) PBTTT-C14 doped in CT-solv (orange) are larger than those in (ii) PBTTT-C14 doped in acetonitrile (red). This indicates that the charge concentration in (iii) PBTTT-C14 doped with CT-solv 180 is higher than that doped in acetonitrile, which is consistent with the variation in conductivity as shown in Fig. 1b. We do not conclude that the doping *via* the dopant-dispersed solvent is superior to that achieved by conventional methods, but do emphasize that this method potentially has comparably excellent doping capability.

The intercalation of F4-TCNQ molecules into the bulk of PBTTT-C14 was verified by XRR measurements. Clear out-of-plane Bragg reflections together with pronounced side fringes

(Laue oscillations) are observed in the pristine PBTTT (black) and doped PBTTT-C14 (i) by F4-TCNQ evaporation (green) and (iii) PBTTT-C14 doped in CT-solv (orange), as shown in Fig. 1d. The lamellar spacing (*d*-spacing) estimated from the Bragg peaks that correspond to (*h*00) diffractions is 21.43 Å for the pristine PBTTT-C14 film, which is consistent with the literature value.<sup>10,13,14</sup> The *d*-spacing for the doped PBTTT-C14 films was expanded by approximately 1.5 Å. The observed elongation of the *d*-spacing by doping supports the diffusion of F4-TCNQ into the PBTTT-C14 polymer network, and the likelihood of F4-TCNQ being stored in-between each lamellae. Note that the observed single and sharp diffraction peaks indicate that the bulk distribution of F4-TCNQ molecules is homogeneous because XRR measurements are essentially sensitive to the bulk, which was also confirmed by the depth variation in the electron density determined from fitting the XRR data. The depth profile of the electron density for (i) pristine PBTTT (black), (ii) PBTTT-C14 doped by evaporation (green), and (iii) PBTTT-C14 doped in CT-solv (orange) is shown in Fig. 1e. The electron density is almost homogeneous along the depth of each film. In addition, the average electron density for the doped PBTTT film is clearly higher than that for the pristine one. The overall XRR measurements further verify the bulk diffusion of F4-TCNQ.

It is interesting to extend the demonstrated doping method to other dopants. The Mo(tfd-COCF<sub>3</sub>)<sub>3</sub> metal-organic complex dopant (shown in Fig. 2a), which is non-evaporative and unstable in polar solvents,<sup>15</sup> was selected. Similar to doping with F4-TCNQ, an efficient charge transfer was confirmed from UV-vis absorption

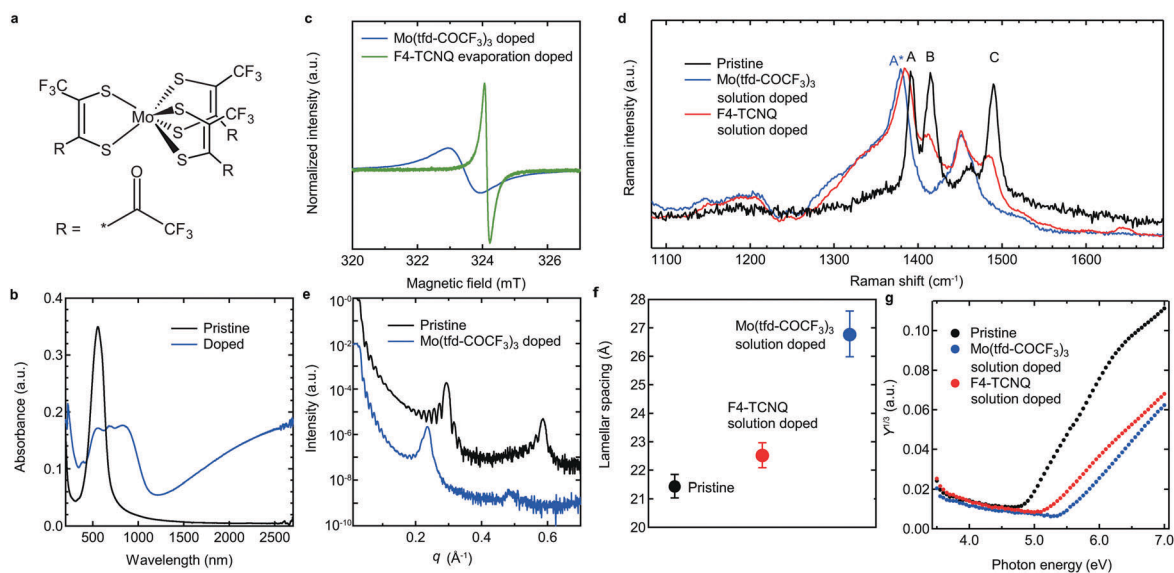


**Fig. 2** (a) Chemical structure of the present metal-organic complex dopant, Mo(tfd-COCF<sub>3</sub>)<sub>3</sub>. (b) UV-vis absorption spectra for the pristine (black) and Mo(tfd-COCF<sub>3</sub>)<sub>3</sub>-doped (blue) PBTTT-C14 thin films. (c) ESR spectra for the Mo(tfd-COCF<sub>3</sub>)<sub>3</sub>-doped (blue) and F4-TCNQ-doped (green) PBTTT-C14 thin films. An external magnetic field was applied perpendicular to the substrate plane. (d) Raman spectra for the pristine (black), F4-TCNQ-doped (red) and Mo(tfd-COCF<sub>3</sub>)<sub>3</sub>-doped (blue) PBTTT-C14 thin films. (e) XRR profile for the pristine (black) and Mo(tfd-COCF<sub>3</sub>)<sub>3</sub>-doped (blue) PBTTT-C14 thin films. (f) Variation in lamellar spacing (*d*-spacing) for the pristine (black), F4-TCNQ-doped (red) and Mo(tfd-COCF<sub>3</sub>)<sub>3</sub>-doped (blue) PBTTT-C14 thin films. (g) Photoemission yield spectroscopy spectra for the pristine (black), F4-TCNQ-doped (red) and Mo(tfd-COCF<sub>3</sub>)<sub>3</sub>-doped (blue) PBTTT-C14 thin films. Photoemission yield, *Y*, is plotted in the form of *Y*<sup>1/3</sup> as a function of the incident photon energy. Doping was performed by immersing the PBTTT-C14 thin film into dopant-dispersed CT-solv 180. All measurements were performed at room temperature.

spectra. Fig. 2b shows the optical absorption spectra for the pristine (black) and Mo(tfd-COCF<sub>3</sub>)<sub>3</sub>-doped PBTTT-C14 (blue). By comparing the UV-vis spectra in solution (see the ESI,† Fig. S2), the peaks at 450 nm and 700 nm are assigned to the energy transition of neutral Mo(tfd-COCF<sub>3</sub>)<sub>3</sub>, which corresponds well to the literature value.<sup>15</sup> After immersion of the pristine PBTTT-C14 into Mo(tfd-COCF<sub>3</sub>)<sub>3</sub> dispersed in CT-solv 180, these neutral absorption peaks become bleached, and a broad peak around 900–1000 nm and a tail around 1200–2700 nm appear, which correspond to PBTTT polaron absorption.<sup>10,13,14</sup> Doping was also confirmed by ESR spectroscopy, as shown in Fig. 2c. In highly-doped conjugated polymers, positive charge carriers should form either localized bipolarons (often referred to as polaron-pairs) or delocalized hole states.<sup>8,13,14,16,17</sup> In either case, spin susceptibility, which contributes to the ESR intensity, is much weaker than the Curie susceptibility for anion spins in dopants. Therefore, the observed ESR signal is attributed purely to anion spins of the dopant molecule, which is evidenced by the measured *g*-factor. The *g*-factor for the PBTTT-C14/F4-TCNQ system (the signal at 324 mT) is in good agreement with that for F4-TCNQ anions (*g* ~ 2.003<sup>13,14</sup>). On the other hand, the *g*-factor for the PBTTT-C14/Mo(tfd-COCF<sub>3</sub>)<sub>3</sub> system (the signal at 323.5 mT) corresponds to that for the Mo(tfd-COCF<sub>3</sub>)<sub>3</sub> anion (*g* ~ 2.008<sup>15</sup>). In addition, ESR spectroscopy can detect the population of unpaired electron spins; the number of spins, *n*<sub>spin</sub>, that contributes to the spin paramagnetic susceptibility can be determined by integrating the first derivative ESR signal. The *n*<sub>spin</sub> for the PBTTT-C14/Mo(tfd-COCF<sub>3</sub>)<sub>3</sub> system is determined to be 8.0 × 10<sup>20</sup> cm<sup>-3</sup>, which is twice as high as that for the PBTTT-C14/F4-TCNQ system (*n*<sub>spin</sub> = 4.1 × 10<sup>20</sup> cm<sup>-3</sup>). The superior doping capability of the Mo(tfd-COCF<sub>3</sub>)<sub>3</sub> dopant was also verified by Raman spectroscopy. The change in the electronic structure of  $\pi$ -conjugated materials is associated with the change in the coordination of the  $\pi$ -core. The non-linear excitation (polaron or bipolaron) will strongly affect the vibrational properties; therefore, Raman spectroscopy is a powerful tool to investigate doped polymers.<sup>18,19</sup> Fig. 2d shows the Raman spectra for the undoped and doped PBTTT-C14 thin films. The observed Raman spectra for the pristine PBTTT-C14 (black), where three Raman modes appear at 1391 (A), 1414 (B), and 1489 (C) cm<sup>-1</sup>, are in good agreement with the literature values.<sup>18,19</sup> After doping, neutral features change significantly; peaks B and C decrease in intensity, and peak A shifts to 1335 (A\*) cm<sup>-1</sup>. These features are assigned to those for the PBTTT cation.<sup>19</sup> A detailed comparison is shown in the ESI† (Tables I and II). For the PBTTT-C14/Mo(tfd-COCF<sub>3</sub>)<sub>3</sub> system, the intensities of neutral peaks B and C become negligibly small, whereas for the PBTTT-C14/F4-TCNQ system, a finite fraction of neutral peaks still remain, which strongly suggests that a higher doping level can be achieved with the Mo(tfd-COCF<sub>3</sub>)<sub>3</sub> acceptor dopant.

The bulk interdiffusion of the Mo(tfd-COCF<sub>3</sub>)<sub>3</sub> molecule, although it was more bulky than F4-TCNQ, was confirmed by XRR measurements (Fig. 2e). Out-of-plane diffraction due to lamellar spacing is observed for the sample doped with Mo(tfd-COCF<sub>3</sub>)<sub>3</sub>, where (*h*00) peaks are shifted to smaller *q* values. Fig. 2f summarizes the variation in lamellar spacing. Elongation of the

lamellar spacing for Mo(tfd-COCF<sub>3</sub>)<sub>3</sub> doping is calculated to be 27.0 Å, which is much larger than that for F4-TCNQ doping. This is apparently due to the bulky nature of the Mo(tfd-COCF<sub>3</sub>)<sub>3</sub> molecule. Due to the bulky nature of Mo(tfd-COCF<sub>3</sub>)<sub>3</sub>, doping is not as homogeneous as for F4-TCNQ and may introduce lattice strain/distortion. However, we conclude that the degree of inhomogeneous doping is not sufficiently deteriorated to diminish the drift mobility of charge carriers, as discussed later. Finally, we discuss the mechanism of efficient doping that is achieved by the Mo(tfd-COCF<sub>3</sub>)<sub>3</sub> molecule. The p-type doping of  $\pi$ -conjugated polymers should involve an oxidation process between the  $\pi$ -core and the acceptor dopant. Recent works highlighted the importance of the energy offset between the HOMO level of p-type organic semiconductors and the LUMO level of acceptor dopants.<sup>9</sup> Essentially, a deep LUMO level in the acceptor dopant will result in strong oxidation. The LUMO level of Mo(tfd-COCF<sub>3</sub>)<sub>3</sub> was estimated to be approximately -5.6 eV,<sup>15</sup> which is far deeper than that of F4-TCNQ (-5.1 eV). This can be verified experimentally by photoemission yield spectroscopy (PYS). PYS counts the net number of photo-emitted electrons per incident photon as a function of a given wavelength. Scanning the photon energy produces a threshold of the photoelectron emission in a vacuum. In metals, the threshold is typically an onset of the work function, while in semiconductors it corresponds to the energy at the top of the valence band. With the reasonable assumption that the transition matrix elements and the escape depth of electrons are constant in a small energy range, the photoemission yield *Y* is expressed with the power law of photon energy, *h* $\nu$ ; *Y* ∝ (*h* $\nu$ )<sup>*n*</sup>, where the exponent *n* = 3 is used when the material is a semiconductor. Fig. 2g plots the photoemission yield *Y*<sup>1/3</sup> as a function of the incident photon energy. *Y*<sup>1/3</sup> increases linearly to the photon energy threshold. The threshold is estimated to be -4.83 eV, -5.20 eV, and -5.43 eV for the pristine PBTTT-C14 (black), PBTTT-C14/F4-TCNQ (red), and PBTTT-C14/Mo(tfd-COCF<sub>3</sub>)<sub>3</sub> (blue), respectively. For the pristine PBTTT-C14, the threshold is identical to the HOMO level, which is slightly shallower than the literature value (-5.0 eV). PYS is sensitive to electrons, even in the trap states; therefore, the observed shift is reasonable and there should be a finite amount of trapped electrons at in-gap states. For doped PBTTT-C14 thin films, such trapped electrons should be taken away from the in-gap state to the acceptor dopant by a charge transfer interaction; therefore, no photo-emitted electrons are yielded. The threshold shift to a higher photon energy direction is attributed to all electrons being removed at the energy threshold. Charge transfer may occur until the onset HOMO level becomes equal to that of the LUMO level of the dopant, and the Fermi level is likely to locate around that point. This argument does not contradict that the LUMO level of Mo(tfd-COCF<sub>3</sub>)<sub>3</sub> (-5.6 eV) is much deeper than that of F4-TCNQ (-5.1 eV). The overall spectroscopy presented here shows that the electron affinity, *i.e.* strong acceptor nature, of the metal-organic dopant gives rise to efficient charge transfer, so that a higher charge density is achieved. Although the demonstrated method with the metal-organic complex dopant has the potential to boost the doping concentration, some open questions remain particularly related to the mechanism of doping *via* solid-state diffusion. For instance, where are the dopants within

the PBTTT's side chain regime, how far from the  $\pi$ -conjugated core do the dopants reside, and what is the arrangement of the dopants? At this point, we prefer not to speculate but merely note that these may have an impact on microscopic charge transfer and charge transport.

Charge transport in conducting polymers has been considered to be hopping transport, and localized polarons undergo multiple hopping processes between localized trap sites.<sup>8</sup> However, coherent charge transport, which is typically referred to as band-like transport, has very recently been demonstrated with observation of the Hall effect,<sup>13,14,20–22</sup> Pauli paramagnetism,<sup>17,23</sup> and Drude-like optical response.<sup>24,25</sup> Magnetotransport measurements, which include measuring longitudinal (merely magnetoresistance) and transverse electromotive forces with the application of an external magnetic field, are particularly useful to probe the degree of coherent charge transport. For longitudinal magnetoresistance measurements, the Anderson localization framework is applicable, even to such conducting polymers.<sup>13,14,26,27</sup> We now elaborate on how molecular doping can impact the coherent charge transport. Longitudinal and transverse magnetotransport measurements were performed using a He gas exchanged cryostat with a superconducting magnet ( $B$  up to 12 T). The doped PBTTT-C14 thin film was patterned into a Hall bar architecture (Fig. 3a and b) by laser etching.  $B$  was ramped up and down to  $\pm 12$  T (Fig. 3c) with application of a constant input current of  $I = 1 \mu\text{A}$ , while longitudinal  $V_{xx}$  and transverse  $V_{xy}$  were monitored simultaneously. A clear  $V_{xy}$  response with respect to

the  $B$  ramp is observed over a wide temperature range (300–40 K) with an excellent signal-to-noise ratio, as shown in Fig. 3d. Devices under the conditions employed in the test were stable during the entire magnetotransport measurements; the conductivity at room temperature was found to recover to the original value after multiple temperature cycles (after 2–3 weeks). The sign of the Hall voltages is consistent with positive carrier (hole) conduction. It should be noted that although coherent charge transport is demonstrated by observation of the Hall effect, the four-terminal conductivity,  $\sigma_{4T}$ , decreases with an increase in temperature  $T$  (Fig. 3e). This is due to a finite amount of grain boundaries in between the metallic domains, which prevents observation of fully metallic conductivity, whereas the electromotive force due to the Hall effect is a summation of the contribution of metallic grains. It should be emphasized that the obtained temperature ( $T$ ) dependence of  $\sigma_{4T}$  can be fit not by a thermal activation model, but by the Efros–Shklovskii variable-range-hopping (ES-VRH) model,  $\sigma = \sigma_0 \exp(T/T_0)^{-1/2}$ , where  $T_0$  is the characteristic temperature. ES-VRH takes into account a soft gap in the density-of-states (DOS) near the Fermi energy due to coulombic interaction between the localized states, and is indicative that such a deviation from the standard VRH fit may be due to finite coherent charge transport together with a higher order of electron–electron interaction associated with a higher charge density.

Hall effect measurement is a powerful tool, not only because it can probe the coherent charge transport, but also because it determines the Hall carrier density,  $R_{\text{H}}$ , and the Hall mobility,  $\mu_{\text{H}}$ . The Hall carrier density, derived from  $n_{\text{Hall}} = (eR_{\text{H}})^{-1}$ , for PBTTT-C14/Mo(tfd-COCF<sub>3</sub>)<sub>3</sub> is almost twice as high as that for PBTTT-C14/F4-TCNQ, which is consistent with the trend in spin concentrations. The Hall carrier densities decrease with temperature, as shown in Fig. 3f. Note that this does not merely mean a reduction of the actual carrier density, but modulation of the (coherence) Hall factor. Based on the assumption that the total charge carrier is equivalent to  $n_{\text{spin}}$  estimated from spin counting in ESR measurements, the Hall factor  $\alpha$  is defined as  $n_{\text{spin}}/n_{\text{Hall}}$  because the previous report has confirmed that the observed optical absorption intensities of polarons for molecular doped PBTTT-C14 are insensitive to the temperature,<sup>13</sup> *i.e.*, the total charge density induced by charge transfer interaction is independent of the temperature. Although the observed Hall effect indicates that band-like charge transport is realized, the presence of hopping carriers may result in a difference between the charge concentrations derived from two separate measurements, because the Hall effect is likely to detect the charge current undergoing the band-like transport, whereas the net of unpaired electrons gives rise to the ESR spectra. The coherence factor,  $\alpha$  at room temperature, is estimated to be 1.7 for PBTTT-C14/F4-TCNQ and 2.0 for PBTTT-C14/Mo(tfd-COCF<sub>3</sub>)<sub>3</sub>. In a Boltzmann transport framework, the Hall factor is predicted to be 1.13 for simple phonon scattering and 1.97 for impurity scattering. Although the observed  $\alpha$  is notably larger than the theoretical limit, this can be explained by taking into account the contribution of hopping carriers. Hall effect measurements in a mixed transport regime with the coexistence of band and

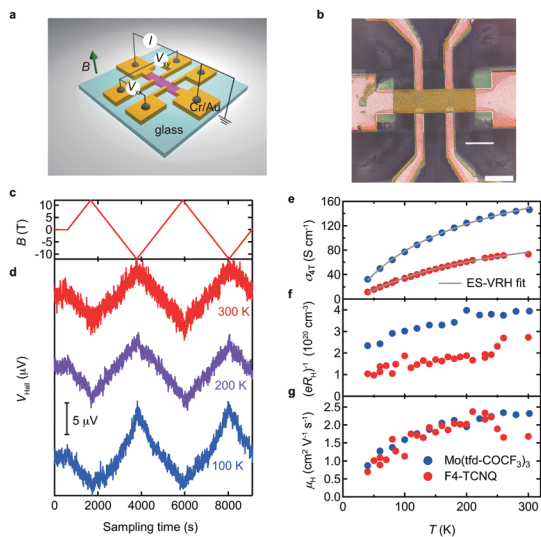


**Fig. 3** (a) Schematic illustration and (b) photograph of the fabricated Hall bar. The longitudinal  $V_{xx}$  and transverse  $V_{xy}$  electromotive forces were monitored simultaneously under the application of a constant dc current,  $I = 1 \mu\text{A}$ . (c) An external magnetic field  $B$  was ramped up to 12 T and down to  $-12$  T. (d) Hall voltage  $V_{\text{Hall}}$  was measured at various temperatures,  $T$ , for the PBTTT-C14/Mo(tfd-COCF<sub>3</sub>)<sub>3</sub> system. (e) Four-terminal conductivity,  $\sigma_{4T}$ , as a function of  $T$ . Solid curves denote computed fits with the Efros–Shklovskii variable-range-hopping model,  $\sigma = \sigma_0 \sim \exp(T/T_0)^{-1/2}$ , where  $T_0$  is the characteristic temperature. (f) Inverse Hall coefficient,  $(eR_{\text{H}})^{-1}$ , as a function of  $T$ . (g) Hall mobility  $\mu_{\text{H}}$  derived from  $\mu_{\text{H}} = R_{\text{H}}\sigma_{4T}$  as a function of  $T$ . Blue and red symbols represent data for PBTTT-C14 doped with Mo(tfd-COCF<sub>3</sub>)<sub>3</sub> and F4-TCNQ, respectively.

hopping charge carriers have been modeled.<sup>28</sup> By adapting this model, we evaluate how many coherent charge carriers undergo band-like transport in doped PBTTT-C14 films (for more details see the ESI†). Given the experimental Hall factor of  $\alpha = n_{\text{spin}}/n_{\text{Hall}} = 2.0$  for PBTTT-C14/Mo(tfd-COCF<sub>3</sub>)<sub>3</sub> and 1.7 for PBTTT-C14/F4-TCNQ, and the assumption of a reasonable hopping mobility  $\mu_{\text{hopping}}$  of  $0.5 \text{ cm}^2 \text{ V}^{-1} \text{ s}^{-1}$  estimated with a field-effect transistor,<sup>29,30</sup>  $\gamma$ , the fraction of band carriers, is estimated to be approximately 0.03 (3%) and 0.20 (20%) for the PBTTT/F4-TCNQ and PBTTT/Mo(tfd-COCF<sub>3</sub>)<sub>3</sub> systems, respectively. We do not further speculate, but would emphasize that the observed coherence factor of more than 2 does not contradict the theory with respect to inorganic semiconductors and metals. It should be noted that the significant increase of the band fraction in the PBTTT/Mo(tfd-COCF<sub>3</sub>)<sub>3</sub> system can be interpreted as carrier filling in the trap states. The trap DOS in organic semiconductors has been studied both experimentally<sup>31,32</sup> and theoretically,<sup>33</sup> where the distribution of the trap DOS is approximated well by an exponential tail. Band-like carrier transport near the mobility edge can be realized rapidly by filling of the trap DOS. In addition, the decrease of the Hall carrier density with the increase of temperature may be due to a rapid increase of hopping contribution. It is more important to conclude that even though the disorder associated with the bulk intercalation of Mo(tfd-COCF<sub>3</sub>)<sub>3</sub> was confirmed by XRR measurements, the Hall mobilities are identical for the two samples with different dopants, which means that the structural disorder in PBTTT-C14/Mo(tfd-COCF<sub>3</sub>)<sub>3</sub> is not sufficiently deteriorated to worsen the charge carrier transport.

The observed coherent charge transport is further verified by a negative longitudinal magnetoresistance, which is due to the weak localization effect that arises from coherent backscattering: a constructive interference between electron waves that traverse along closed paths in opposite loops. The negative magnetoresistance (equally positive magnetoconductance,  $G$ ) is measured by reducing the backscattering because an external magnetic field flux can break

the symmetry. The weak localization effect is applicable even to disordered conducting polymers.<sup>13,14,26,27</sup> This, in principle, suggests how the charge carrier transport is coherent, which is supported by the Hikami–Larkin–Nagaoka (HLN) model.<sup>34</sup> The  $B$ -dependence of differential conductance ( $\Delta G(B) = G(B) - G(0)$ ) at various  $T$  is shown in Fig. 4a. The observed magnetoconductance is parabolic with respect to the applied  $B$ , and is fit by the HLN model,  $\Delta G(B) = G_0/24(B/B\phi)^2$ , where  $G_0 = e^2/2\pi^2\hbar$ .  $B\phi$  is the characteristic magnetic field for which the backscattering loses its phase, and is the only fitting parameter, as shown in Fig. 4b. The inelastic scattering length ( $\lambda\phi$ ), which is identical to the weak localization length, can be determined directly from the equation  $\lambda\phi = \sqrt{\hbar/4eB\phi}$ , which is shown in Fig. 4c. The  $\lambda\phi$  for PBTTT-C14/Mo(tfd-COCF<sub>3</sub>)<sub>3</sub> is 10–20% higher than that for PBTTT-C14/F4-TCNQ, which further supports that the higher degree of doping realized by the metal–organic complex dopant promotes band-like transport.

## Conclusions

The results presented here demonstrate that the molecular implantation concept, which is an ideal hybridization of host–guest molecules, can be extended to a fully solution process. It is particularly important that the use of a dopant-dispersed orthogonal solvent can be extended to dopant variations, such as non-evaporative, insoluble metal–organic complexes. One of the highest doping levels with the Mo(tfd-COCF<sub>3</sub>)<sub>3</sub> dopant in organic semiconductors is achieved with coherent band-like transport, which was verified by magnetotransport measurements. We would like to emphasize that even though such a bulky dopant is intercalated into the polymer network, the two-dimensional charge transport nature, which is essential to realize high mobility in host polymers, is not deteriorated. The novel route for molecular doping presented in this work is expected to promote development not only in material sciences, but also in device applications.

## Experimental

### Materials and device fabrication

A standard thiophene-based semiconducting polymer, PBTTT-C14, with an estimated molecular weight of  $50\,000 \text{ g mol}^{-1}$ , was purchased from Sigma-Aldrich. A metal-oxide dopant, Mo(tfd-COCF<sub>3</sub>)<sub>3</sub>, was also purchased from Sigma-Aldrich, and was used without any purification. The fluorinated solvent, CT-solv 180, which is composed of 90–95% (C<sub>4</sub>F<sub>9</sub>)<sub>3</sub>N, was purchased from Asahi Glass. Since the solvents used in this paper, acetonitrile and CT-solv 180, are often utilized to form a gate dielectric layer (the former for poly(methyl methacrylate) and the latter for CYTOP) on top of polymer semiconductors,<sup>35</sup> they are known to be orthogonal to PBTTT and do not cause any fatal damage to thin films of PBTTT. 0.05 wt% of Mo(tfd-COCF<sub>3</sub>)<sub>3</sub> was added to CT-solv 180 and the solution was sonicated for 30 min to uniformly disperse Mo(tfd-COCF<sub>3</sub>)<sub>3</sub> into CT-solv 180. PBTTT-C14 thin films were prepared by spin-coating from 1.0 wt% 1,2-dichlorobenzene at 2000 rpm for 60 s and then annealing at

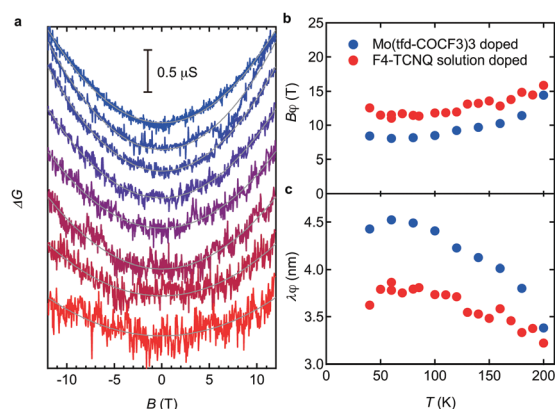


Fig. 4 (a)  $B$  dependence of differential conductance,  $\Delta G(B) = G(B) - G(0)$ , at various  $T$  (40–180 K from top to bottom).  $B$  was applied perpendicular to the substrate plane. The solid curves represent the computed fit based on the HLN model. (b)  $T$  dependence of the extracted  $B\phi$  and (c) the inelastic scattering length  $\lambda\phi$ .

180 °C for 30 min. The resulting 45 nm thick PBTTT-C14 thin film was immersed in dopant dispersed CT-solv 180 at 60 °C for 30 min. The samples were used for UV-vis, ESR, XRR, and PYS measurements.

The devices were fabricated on 0.7 mm thick Eagle glass substrates that were pre-cleaned by sonication in acetone and isopropanol. Cr (3 nm) and Au (40 nm) electrodes were deposited by thermal evaporation through a shadow mask to form a channel length ( $L$ ) and channel width ( $W$ ) of 550  $\mu\text{m}$  and 430  $\mu\text{m}$ , respectively. After the metallization processes, the devices were further cleaned with acetone and isopropanol. The PBTTT-C14 thin film was formed in a similar manner to that for characterization. After solution doping, the doped PBTTT-C14 channel was patterned into a Hall bar geometry by laser etching.

### Spectroscopy and magnetotransport measurements

UV-vis absorption measurements were conducted with a UV-vis spectrometer (JASCO V-670ST). ESR measurements were performed with a JEOL JES310 spectrometer. The spin susceptibility was determined by integrating the first derivative signal twice, where a manganese marker was used as a reference. PYS was performed with a PYS-202 spectrometer (Sumitomo Heavy Industries Co.). Raman spectra were recorded with a Horiba HR-evolution confocal Raman microscope using a HeNe (633 nm) laser. XRR was performed with a GE XRD 30033 TT diffractometer with Cu K $\alpha$ 1 radiation ( $\lambda = 0.15406$  nm). The  $d$ -spacing was estimated from  $d = 2\pi/q_{(100)}$ . Magnetotransport measurements were performed using a He-gas exchanged cryostat with a superconducting magnet. Both the longitudinal and transverse electromotive forces were monitored simultaneously with application of a dc current of 1  $\mu\text{A}$  while the magnetic field was swept from 12 T to  $-12$  T at a rate of 0.4 T  $\text{min}^{-1}$ .

### Conflicts of interest

There are no conflicts to declare.

### Acknowledgements

This work was supported by the PRESTO program ‘‘Hyper-nano-space design toward Innovative Functionality’’ through a Grant-in-Aid (No. JPMJPR151E) from the Japan Science and Technology Agency (JST).

### References

- H. Shirakawa, *Angew. Chem., Int. Ed.*, 2001, **40**, 2574–2580.
- A. MacDiarmid, J. Chiang, A. Richter and A. J. Epstein, *Synth. Met.*, 1987, **18**, 285–290.
- C. J. Brabec, N. S. Sariciftci and J. C. Hummelen, *et al.*, *Adv. Funct. Mater.*, 2001, **11**, 15–26.
- E. Frackowiak, V. Khomenko, K. T. Jurewicz, K. Lota and F. Beguin, *J. Power Sources*, 2006, **153**, 413–418.
- M. Gerard, A. Chaubey and B. Malhotra, *Biosens. Bioelectron.*, 2002, **17**, 345–359.
- O. Bubnova, Z. U. Khan, A. Malti, S. Braun, M. Fahlman, M. Berggren and X. Crispin, *Nat. Mater.*, 2011, **10**, 429–433.
- K. Ando, S. Watanabe, S. Mooser, E. Saitoh and H. Sirringhaus, *Nat. Mater.*, 2013, **12**, 622–627.
- A. J. Heeger, S. Kivelson, J. Schrieffer and W.-P. Su, *Rev. Mod. Phys.*, 1988, **60**, 781.
- B. Lüssem, C.-M. Keum, D. Kasemann, B. Naab, Z. Bao and K. Leo, *Chem. Rev.*, 2016, **116**, 13714–13751.
- J. E. Cochran, M. J. Junk, A. M. Glaudell, P. L. Miller, J. S. Cowart, M. F. Toney, C. J. Hawker, B. F. Chmelka and M. L. Chabinye, *et al.*, *Macromolecules*, 2014, **47**, 6836–6846.
- S. N. Patel, A. M. Glaudell, D. Kiefer and M. L. Chabinye, *ACS Macro Lett.*, 2016, **5**, 268–272.
- C. Y. Kao, B. Lee, L. S. Wielunski, M. Heeney, I. McCulloch, E. Garfunkel, L. C. Feldman and V. Podzorov, *Adv. Funct. Mater.*, 2009, **19**, 1906–1911.
- K. Kang, S. Watanabe, K. Broch, A. Sepe, A. Brown, I. Nasrallah, M. Nikolka, Z. Fei, M. Heeney and D. Matsumoto, *et al.*, *Nat. Mater.*, 2016, **15**, 896.
- R. Fujimoto, S. Watanabe, Y. Yamashita, J. Tsurumi, H. Matsui, T. Kushida, C. Mitsui, H. T. Yi, V. Podzorov and J. Takeya, *Org. Electron.*, 2017, **47**, 139–146.
- S. K. Mohapatra, Y. Zhang, B. Sandhu, M. S. Fonari, T. V. Timofeeva, S. R. Marder and S. Barlow, *Polyhedron*, 2016, **116**, 88–95.
- K. Marumoto, Y. Muramatsu, Y. Nagano, T. Iwata, S. Ukai, H. Ito, S.-I. Kuroda, Y. Shimoi and S. Abe, *J. Phys. Soc. Jpn.*, 2005, **74**, 3066–3076.
- H. Tanaka, M. Hirate, S. Watanabe and S.-I. Kuroda, *Adv. Mater.*, 2014, **26**, 2376–2383.
- Y. Furukawa, K. Akiyama, I. Enokida and J. Yamamoto, *Vib. Spectrosc.*, 2016, **85**, 29–34.
- C. Francis, D. Fazzi, S. B. Grimm, F. Paulus, S. Beck, S. Hillebrandt, A. Pucci and J. Zaumseil, *J. Mater. Chem. C*, 2017, **5**, 6176–6184.
- Y. Yamashita, J. Tsurumi, F. Hinkel, Y. Okada, J. Soeda, W. Zajaczkowski, M. Baumgarten, W. Pisula, H. Matsui and K. Müllen, *et al.*, *Adv. Mater.*, 2014, **26**, 8169–8173.
- S. P. Senanayak, A. Ashar, C. Kanimozhi, S. Patil and K. Narayan, *Phys. Rev. B: Condens. Matter Mater. Phys.*, 2015, **91**, 115302.
- S. Wang, M. Ha, M. Manno, C. D. Frisbie and C. Leighton, *Nat. Commun.*, 2012, **3**, 1210.
- S. Ikehata, J. Kaufer, T. Woerner, A. Pron, M. Druy, A. Sivak, A. Heeger and A. MacDiarmid, *Phys. Rev. Lett.*, 1980, **45**, 1123.
- K. Lee, S. Cho, S. H. Park, A. Heeger, C.-W. Lee and S.-H. Lee, *Nature*, 2006, **441**, 65–68.
- Y. Chang, K. Lee, R. Kiebooms, A. Aleshin and A. Heeger, *Synth. Met.*, 1999, **105**, 203–206.
- D. Farka, H. Coskun, J. Gasiorowski, C. Cobet, K. Hingerl, L. M. Uiberlacker, S. Hild, T. Greunz, D. Stifter and N. S. Sariciftci, *et al.*, *Adv. Electron. Mater.*, 2017, DOI: 10.1002/aelm.201700050.
- S. Zanettini, J. Dayen, C. Etrillard, N. Leclerc, M. V. Kamalakar and B. Doudin, *Appl. Phys. Lett.*, 2015, **106**, 063303.
- H. Yi, Y. Gartstein and V. Podzorov, *Sci. Rep.*, 2016, **6**, 23650.

- 29 I. McCulloch, M. Heeney, C. Bailey, K. Genevicius, I. MacDonald, M. Shkunov, D. Sparrowe, S. Tierney, R. Wagner and W. Zhang, *et al.*, *Nat. Mater.*, 2006, **5**, 328–333.
- 30 C. Wang, L. H. Jimison, L. Goris, I. McCulloch, M. Heeney, A. Ziegler and A. Salleo, *Adv. Mater.*, 2010, **22**, 697–701.
- 31 J. Rivnay, R. Noriega, J. E. Northrup, R. J. Kline, M. F. Toney and A. Salleo, *Phys. Rev. B: Condens. Matter Mater. Phys.*, 2011, **83**, 121306.
- 32 D. Venkateshvaran, M. Nikolka, A. Sadhanala, V. Lemaire, M. Zelazny, M. Kepa, M. Hurhangee, A. J. Kronemeijer, V. Pecunia and I. Nasrallah, *et al.*, *Nature*, 2014, **515**, 384.
- 33 T. Liu and A. Troisi, *Adv. Funct. Mater.*, 2014, **24**, 925–933.
- 34 S. Hikami, A. I. Larkin and Y. Nagaoka, *Prog. Theor. Phys.*, 1980, **63**, 707–710.
- 35 N. Zhao, Y.-Y. Noh, J.-F. Chang, M. Heeney, I. McCulloch and H. Sirringhaus, *Adv. Mater.*, 2009, **21**, 3759–3763.